Excitation protocols for nonlinear phononics in bismuth and antimony

Anubhab Haldar [1] Zhengjie Huang,[2] Xuedan Ma,[2,3,4] Pierre Darancet [2,3,*] and Sahar Sharifzadeh [1,5,†]

[1]*Department of Electrical and Computer Engineering, Boston University, Boston, Massachusetts 02215, USA*
[2]*Center for Nanoscale Materials, Argonne National Laboratory, Argonne, Illinois 60439, USA*
[3]*Northwestern Argonne Institute of Science and Engineering, Evanston, Illinois 60208, USA*
[4]*Consortium for Advanced Science and Engineering, The University of Chicago, Chicago, Illinois 60637, USA*
[5]*Division of Materials Science and Engineering, Boston University, Boston, Massachusetts 02215, USA*

We study the optical generation and control of coherent phonons in elemental bismuth (Bi) and antimony (Sb) using a classical equation of motion informed by first-principles calculations of the potential energy surface and the frequency-dependent macroscopic dielectric function along the zone-centered optical phonon coordinates. Using this approach, we demonstrate that phonons with the largest optomechanical couplings also have the strongest degree of anharmonicity among the zone-centered modes, a result of the broken-symmetry structural ground state of Bi and Sb. We show how this anharmonicity, explaining the light-induced phonon softening observed in experiments, prevents the application of standard phonon-amplification and annihilation protocols. We introduce a simple linearization protocol that extends the use of such protocols to the case of anharmonic phonons in broken-symmetry materials, and demonstrate its efficiency at high displacement amplitudes. Our formalism and results provide a path for improving optical control in nonlinear phononics.

I. INTRODUCTION

Coherent interactions between electromagnetic waves and extended vibrational degrees of freedom in solids (phonons) enable the stabilization of highly nonthermal states of matter with potentially desirable properties [1]. Such interactions have been observed using femtosecond laser pulses in a wide variety of materials over the past 50 years, including oxides [2], transition metal dichalcogenides [3], elemental pnictogens [4–11], and have been leveraged for control of vibrational dynamics [7,10,12], nonequilibrium structural phase transitions [2,3], and to modulate the nonlinear susceptibility [13–15].

Microscopically, the coherent coupling between electromagnetic waves and vibrational degrees of freedom is generally understood as a consequence of vibration-induced changes in the dielectric susceptibility in the frequency range of the pump laser [16]. Such changes can be the result of processes involving Raman scattering [17], infrared phonons [18,19], ionic Raman scattering [14,19], or infrared resonant Raman scattering [15]. For opaque materials, an early phenomenological theory was the displacive excitation of coherent phonons (DECP) [20], later shown to be a special case of impulsive stimulated Raman scattering [8]. The DECP model can explain the oscillatory cosinelike dependence of optical reflectivity upon excitation by impulsive laser sources by considering the change in the electron density in the presence of a coherently excited phonon. Such

conclusions were also verified using a density-matrix-based model [21] in the case of antimony. In contrast to this deep theoretical understanding of the underlying coupling mechanism, however, most illumination protocols leading to the stabilization of nonequilibrium phases have been discovered through trial-and-error approaches. A primary reason is the lack of quantitative methods capable of treating the full, anharmonic, potential energy surface and the driving force on an equal footing. To this end, first-principles approaches using Born-Oppenheimer [15] or Ehrenfest [22,23] dynamics in conjunction with time-dependent density functional theory (TDDFT) provide an important opportunity in the understanding and control of these systems.

In this paper, using a fully first-principles-informed classical model, we study light-induced structural dynamics in bismuth (Bi) and antimony (Sb), two broken-symmetry elemental solids, which have been extensively studied experimentally and show clear macroscopic evidence of coherent phonons [9,11,16,24–27]. For these systems, we calculate the potential energy surface (PES) and the frequency-dependent dielectric function within density functional theory (DFT) and TDDFT, respectively, along the full range of phonon amplitudes Q_i, for the zone-centered optical modes. With these parameters as input, we perform a classical Born-Oppenheimer dynamics simulation with a nonlinear force term explicitly depending on phonon coordinates and electric field magnitude. Using this approach, we demonstrate that the A_{1g} phonon mode, the mode with the largest optomechanical couplings in Bi and Sb, also has the strongest degree of anharmonicity among the zone-centered modes, explaining the light-induced phonon softening observed in experiments. Such anharmonicity results from the broken-symmetry structural ground state
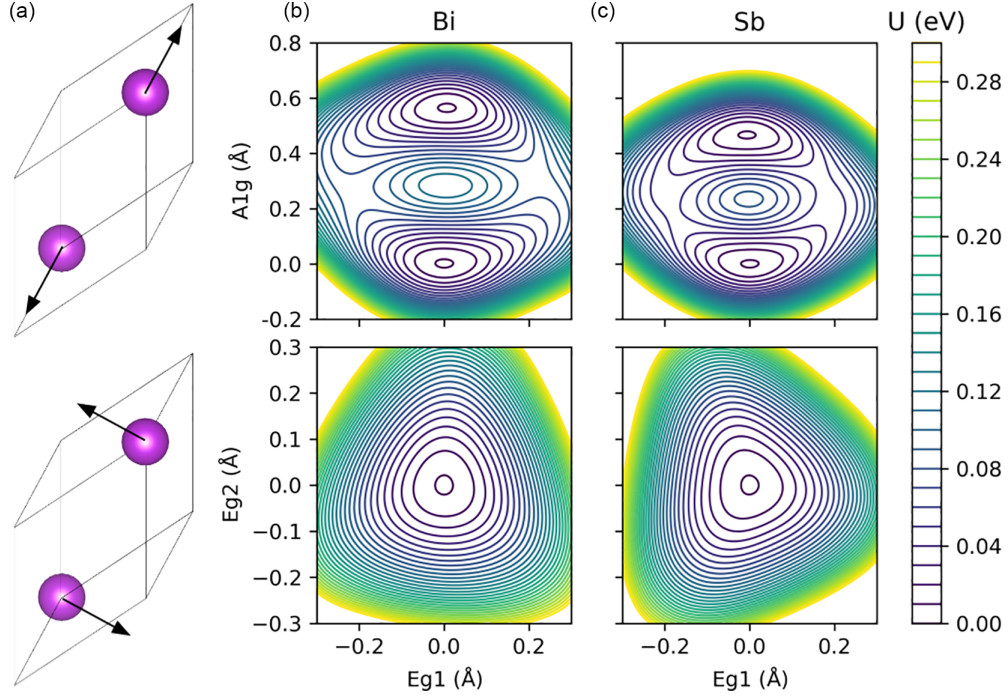
*pdarancet@anl.gov
†ssharifz@bu.edu

FIG. 1. (a) The orthorhombic unit cell of Bi and Sb with the motion of atoms associated with the A_{1g} (top) and one of two degenerate E_g phonon modes (bottom). In (b) and (c), we show the potential energy surface with atoms moved along pairs of normal modes, with the third normal mode set to $Q = 0$. Coordinates (0,0) correspond to the ground-state configuration. Potential energy (U) is in units of eV/unit cell (2 atoms).

and prevents the application of standard phonon-amplification and annihilation protocols based on a period/half-period pulse train. We introduce a simple linearization protocol that extends the use of phonon-annihilation and amplification protocols to the case of such phonons, and demonstrate its efficiency at high displacement amplitudes.

II. RESULTS

Briefly, the set of phonon coordinates $Q_i(t)$ (where i is the mode index) at an instant t are evolved on the Born-Oppenheimer energy surface, using the following instantaneous forces $\mathbf{F}(\mathbf{Q}_i, t)$,

$$\mathbf{F}(\mathbf{Q}_i, t) = -\left.\frac{dU}{d\mathbf{Q}}\right|_{\mathbf{Q}=\mathbf{Q}_i(t)} + \mathbf{E}^*(\omega, t) \left.\frac{d\chi_\mathbf{Q}(\omega)}{d\mathbf{Q}}\right|_{\mathbf{Q}=\mathbf{Q}_i(t)} \mathbf{E}(\omega, t),$$

$$(1)$$

where U is the total energy without illumination, $\mathbf{E}(\omega, t) = \mathbf{A}(t)e^{i\omega t} \simeq \mathbf{A}(t)$ is the electric field of the light approximated by its slowly varying (when compared to $1/\omega$) amplitude $\mathbf{A}(t)$, and $\chi_\mathbf{Q}(\omega)$ is the macroscopic polarizability tensor of the system at coordinates $\mathbf{Q}$. Both U and $\chi_\mathbf{Q}$ are obtained from DFT and TDDFT calculations on a dense grid of configurations [28–31], and interpolated using a radial basis interpolation on that grid following the procedure detailed in the Supplemental Material [32,33].

Both Bi and Sb form crystals with an orthorhombic unit cell consisting of two atoms with a threefold symmetry around the body diagonal (see Fig. 1). Thus, there are two point group symmetries associated with the three optical phonon modes of interest in this work: the fully symmetric A_{1g} mode, corresponding to an out-of-phase displacement of the two

atoms along their bond, and two doubly degenerate E_g modes, corresponding to displacements normal to that bond. As shown in Ref. [16], only the Raman tensor of A_{1g} is diagonal (symmetric under all orthorhombic point group operations), in contrast with the off-diagonal Raman tensor of the E_g modes, suggesting the latter can only be excited via second-order effects.

Figure 1 presents the PES as a function of atomic motion along the A_{1g} and E_g optical zone-centered phonon modes of Bi and Sb. Both materials have a characteristic double-well potential along their A_{1g} direction with both minima being structurally equivalent. This energy profile is a consequence of the broken-symmetry ground state due to a Peierls-like distortion from a high-symmetry configuration (at $Q_{A_{1g}} \simeq 0.3$ Å), where no Bi-Bi and Sb-Sb bond is elongated. The predicted dimerization energy (energy difference between a minimum and the high-symmetry configuration per 2-atom unit cell) for Sb ($\sim$100 meV) is lower than that for Bi ($\sim$140 meV), indicating that Bi has a stronger tendency towards dimerization, and, accordingly, that the A_{1g} modes in Sb near the energy minima are more anharmonic. In contrast, E_g modes retain a near-harmonic character for displacements $Q_{E_g} \simeq \pm 0.2$ Å with the trigonal deviation caused by the threefold symmetry of the lattice. In the limit of small displacements, we predict the phonon frequencies for the A_{1g} and E_g modes to be, respectively (3.06, 2.47) THz for Bi and (4.31, 2.77) THz for Sb, in good agreement with the experimental values of (2.9, 2.2) and (4.5, 3.5) THz [5].

A simple quantification of the mode anharmonicity can be obtained by fitting the energy versus displacement curve for a single phonon coordinate (the two others being fixed

TABLE I. Third-order (Q^3) and fourth-order (Q^4) fit coefficients of the potential energy surface with displacements along the three phonon normal modes for both Bi and Sb.

	Bi		Sb	
	Q^3 (eV/Å³)	Q^4 (eV/Å⁴)	Q^3 (eV/Å³)	Q^4 (eV/Å⁴)
A_{1g}	−4.3	−8.6	8.6	−21.6
E_{g1}	0.6	2.8	2.2	7.1
E_{g2}	−2.1	1.9	0.9	8.0

to $Q = 0$, neglecting intermode coupling) by a higher-order polynomial: For A_{1g}, E_{g1}, and E_{g2}, respectively, we obtain the following third-order and fourth-order coefficients for Bi and Sb as shown in Table I. The magnitude of these coefficients is associated with two main effects: First, as the force depends on the distance from the equilibrium position, the phonon frequency becomes amplitude dependent, an effect observed experimentally for the A_{1g} mode [10] in Bi. Second, as the third- and fourth-order force constants correspond to three- and four-phonon interactions, these coefficients are related to the onset of higher harmonics at integer multiples of the original frequencies. Beyond these two effects, our approach also contains cross-phonon terms (e.g., $Q_{A_{1g}} Q_{E_g}^2$) that transfer energy across the different branches, which enable selective excitation of originally degenerate phonon modes (though observing this effect can be complicated by the large decay rates of these modes [7]).

To analyze the effect of the mode anharmonicity on the light-induced dynamics, we conduct transient spectroscopy experiments on bismuth at various pump laser intensities. All experimental details are indicated in the Supplemental Material [32]. We then extract the frequency domain response from the pump-probe traces, showing the pump-intensity-dependent shift of the frequency of the A_{1g} phonon response. At low fluence, the coherent phonon frequency is in good agreement [5] with the one measured through Raman spectroscopy. However, and as shown in Fig. 2(a), higher laser fluences lead to a softening of the A_{1g} phonon frequency, in agreement with prior measurements [10,11,34]. As discussed above, such behavior can be explained by the larger displacement at higher fluences, giving rise to larger anharmonicity. We also note the appearance of second harmonics for a laser power of 0.2 mW (see Supplemental Material [32]), while the E_g modes are predicted and observed to be negligibly excited for nonpolarized light. We note that for our system, the phonon frequencies are well separated and so we do not expect multiple peaks in the reflectivity spectrum. [35]

As we will now show, the phonon softening has important consequences for phonon excitation protocols. We illustrate this point by simulating the light-induced dynamics caused by a simple, two-pulse protocol, shown in Fig. 2(b), where the two pulses are separated by a delay expressed as multiples of the phonon time period. For purely harmonic potentials, pulses sent at integer phonon time periods lead to constructive interference between the two coherent excitations,
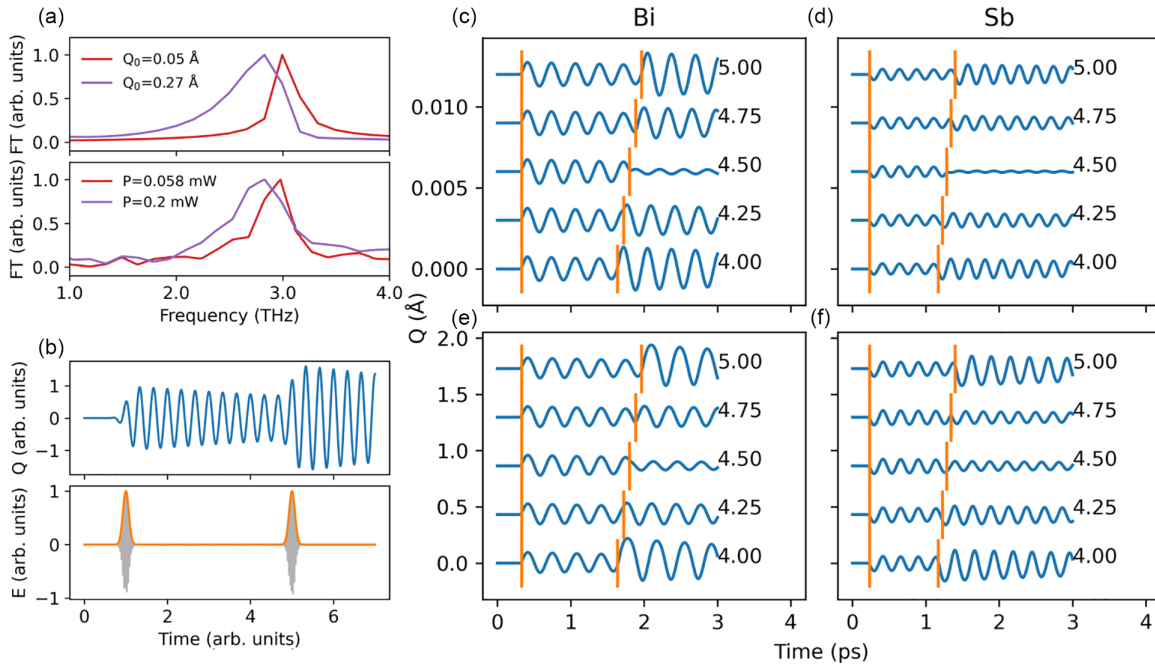

FIG. 2. (a) Comparison of experiment (bottom) and theory (top) in the extracted frequency of the coherent phonon within Bi via the Fourier transform of the reflectivity trace at two different laser fluences/simulated amplitude. The theoretical displacement is chosen to reproduce the frequency shift observed in experiment. (b) Schematic of a two-pulse experiment and a resulting oscillatory trace. (c)–(f) show the two-pulse dynamics with a second pulse placed a half-integer time period away in order to fully destructively interfere with the first pulse within the harmonic approximation. (c) and (d) show waterfall plots of the trajectories simulated for low pulse powers in Bi and Sb. Q is the amplitude along the A_{1g} coordinate, and the plots are shifted by a different constant for the different trajectories. Different trajectories are labeled by the time delay in units of the harmonic phonon time period (4.0–5.0 T). (e) and (f) show the same trajectories generated by a high pulse powers as defined in the text. A phenomenological damping rate of 0.1 THz was added to the simulations.

i.e., phonon amplification, while pulses sent at half-integer periods lead to destructive interference, i.e., phonon annihilation [7,10,36]. Accordingly, and as shown in Figs. 2(c) and 2(d), excitations at weak electric field amplitude (4.2 and 2.1 MV/m for Bi and Sb, respectively, corresponding to a peak laser power of 2.9 and 1.5 kW, respectively; see Supplemental Material [32]) result in low-amplitude phonon oscillations, and such phonons can be amplified and annihilated at times based on their integer/half-integer oscillation periods.

However, at the stronger electric field amplitude of $\sim$67 and $\sim$54 MV/m for Bi and Sb, respectively (corresponding to a peak laser power of 748 and 486 kW, respectively), the amplitude of the oscillation ($\sim$0.1–0.2 Å) leads to significant anharmonic effects: As shown in Figs. 2(e) and 2(f), the corresponding oscillation period becomes longer, with four full oscillations taking $\sim$4.1 harmonic oscillation periods. Consider the frequency ω at any intensity to take the form

$$\omega = \omega_0 + \delta\omega[A(t)], \qquad (2)$$

where ω_0 is the low-amplitude phonon frequency, respectively, and $\delta\omega$ is the change in frequency due to anharmonicity, with $\delta\omega[A(t)] \simeq 0.2$ THz at $\simeq 0.2$ Å.

We note that an analytical solution to Eq. (2) is possible provided a known analytical form of the PES. For example, Ref. [37] introduced an expression for $\delta\omega[A(t)]$ for the case of hexagonal boron nitride, where the potential energy surface along the infrared-active phonon coordinates can be accurately described by a fourth-order polynomial.

Instead, we now propose a simple correction to standard protocols that enable their extension to the anharmonic regime. We use an approximation inspired by the amplitude-dependent harmonic approximation as described in Ref. [38]. Here, we approximate the PES by a harmonic potential *dependent on the amplitude*, i.e., $E(\mathbf{Q}) = 1/2 \frac{dU}{d\mathbf{Q}}|_{\mathbf{Q}} |Q|^2$. Under this assumption, the amplitude-dependent force constant is an instantaneously linear approximation to the restoring forces that the oscillator feels over its trajectory. We refer to this protocol as the optimal linear approximation of forces (OLAF). Importantly, by enabling $\frac{dU}{d\mathbf{Q}}|_{\mathbf{Q}} \neq \frac{dU}{d\mathbf{Q}}|_{-\mathbf{Q}}$, OLAF can in principle reproduce the large and amplitude-dependent asymmetry of the PES along the A_{1g} coordinate. Along a given coordinate, we obtain the amplitude-dependent restoring force by minimization of

$$\mathbf{F}_{\text{OLAF}}(A) = \min[||\mathbf{F} - \mathbf{F}_{\text{truth}}(|Q| < A)||_2], \qquad (3)$$

for Q in $[0, +A]$ at positive Q and Q in $[-A, 0]$ at negative Q, with A being the instantaneous amplitude. Importantly and as shown in the Supplemental Material (Fig. S2 [32]), these values can also be approximated by independently fitting the half period at positive and negative amplitude. Equation (3) can be understood as an approximating the full potential energy surface defined by $\mathbf{F}_{\text{truth}}$ by a series of amplitude-dependent harmonic potentials $\mathbf{F}_{\text{OLAF}}(A)$ extracted from each half period of oscillation.

We note that this approach has key differences when compared with temperature-dependent effective potentials (TDEPs). TDEP studies have generally focused on the study of acoustic modes, which have a different behavior than optical modes that we study here. Additionally, it is important to note that while we neglect thermal expansion, we expand the potential energy surface at higher orders than the harmonic approximation, which TDEP approximates.

Figure 3(a) presents the difference between the harmonic approximation and the OLAF approach along the A_{1g} coordinate, with the amplitude varied in the $\pm$ regime as was found to agree well with experiment. For OLAF, we plot the second-order polynomial fits to the PES for Q within $\pm$20 pm, and contrast it to the ground truth, a harmonic fit obtained analytically as a second derivative at $Q = 0$, and the OLAF protocol under the constraint of $\frac{dU}{d\mathbf{Q}}|_{\mathbf{Q}} = \frac{dU}{d\mathbf{Q}}|_{-\mathbf{Q}}$ (labeled as symmetric OLAF). As expected, the harmonic approximation deviates from the ground truth as the amplitude approaches the high-symmetry configuration. While a symmetrized amplitude-dependent effective harmonic potential can extend the domain of validity of the harmonic approximation, this is accomplished by shifting the energy minimum away from equilibrium towards more positive amplitudes for larger displacement. In contrast, OLAF conserves the correct position of the energy minimum and accounts for the asymmetry between positive and negative amplitudes. We note, however, that OLAF can only indirectly reproduce the concavity of the PES at positive amplitudes through a set of rapidly decaying force constants.

Importantly, our amplitude-dependent harmonic approximation leads to a trajectory with a smaller deviation from the true trajectory over a longer period of time as shown in Fig. 3(b). We note that the softening of the phonon mode can be seen through the change in oscillation time period in the truth as well as the OLAF trajectory, but is missing from the harmonic approximation. Another important consequence of the energy profile along the A_{1g} coordinate is the shorter half period for the negative amplitudes as compared to the positive amplitudes, as well as their inverse behaviors at large amplitudes: As shown in Fig. S2, the negative-amplitude half periods are slightly shortened at high amplitude, while the positive-amplitude half periods are increased. This phenomenon is captured quantitatively by the asymmetric fit, and can also be derived by measuring the lengths of the half periods through the zero crossings of the experimental spectroscopic traces.

The consequences of these approximations in determining two-pulse protocols are shown in Fig. 3(c), for a standard phonon-annihilation protocol shining a second pulse 2.75 periods after an amplitude maximum efficient at small amplitude: Over the course of those 15 pm oscillations, the phase accumulated in the harmonic approximation considerably reduces the effectiveness of the protocol. In contrast, the 2.75 periods predicted by OLAF closely match the numerically optimized result. We note that the asymmetry between the positive and negative amplitudes is enough to significantly lower the efficiency of the symmetrized OLAF protocol at those amplitudes, indicating that our asymmetric protocol is particularly suited to broken-symmetry materials.

We define the figure of merit corresponding to the destructive interference as

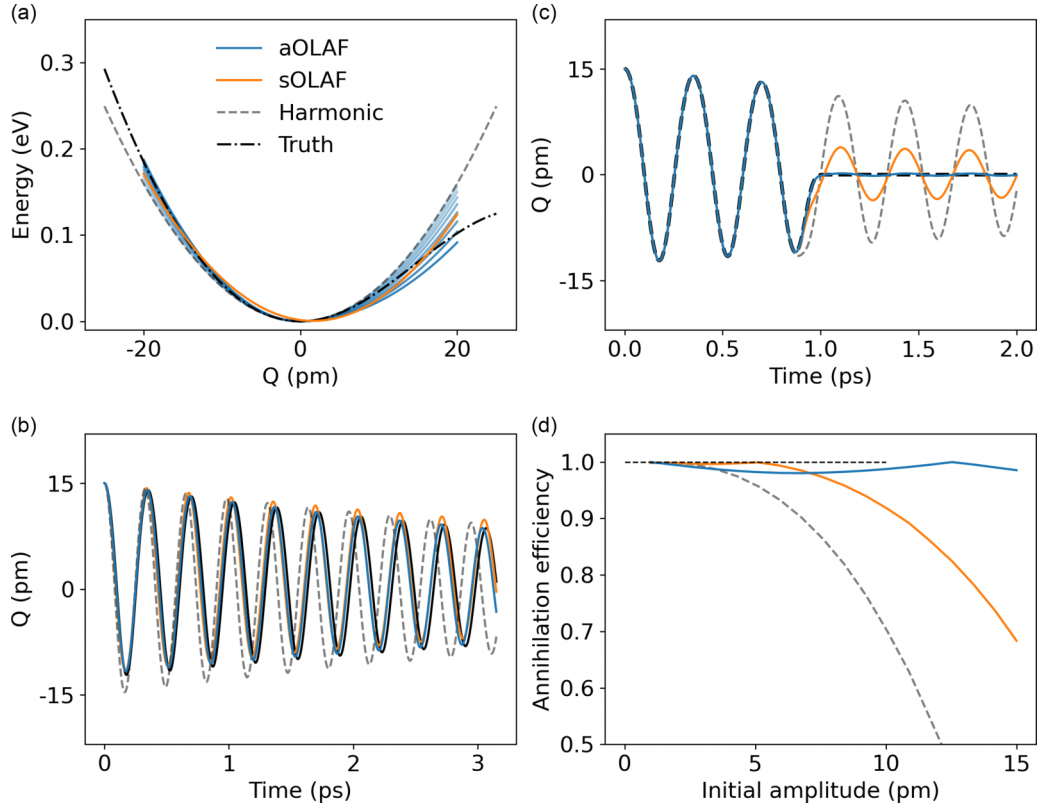$$\mathcal{F} = 1 - \frac{A_{2p}}{A_0}, \qquad (4)$$

FIG. 3. (a) The calculated PES along the A_{1g} coordinate compared with the harmonic approximation of the PES, the symmetric (s), and asymmetric (a) effective harmonic approximation (OLAF) introduced in the text. For aOLAF, we plot nine lines with differing amplitudes uniformly spaced by 2.5 pm and ranging from 0 to 20 pm, shaded such that the darker the colors correspond to larger amplitudes. (b) Phonon trajectories initialized with an amplitude of 10 pm, corresponding to the ground truth PES, harmonic, and two OLAF approximations. (c) Coherent phonon annihilation via two-pulse excitation within the three approximations for an initial amplitude of 15 pm. (d) The proportion of the oscillation amplitude that is removed after the second pulse.

where A_{2p} is the time-averaged norm of the oscillations after the second pulse and A_0 is the same quantity without the second pulse. In the case of the full PES, the annihilation efficiency would be 1. However, for the harmonic approximation the efficiency decays from 0.9 at 5 pm to <0.7 at 10 pm. The OLAF effective harmonic approximation improves the validity, extending the range of annihilation up to 10 pm. In contrast, the asymmetric OLAF protocol enables full annihilation efficiency across this range of amplitudes.

Modeling oscillations with amplitude-dependent frequencies and the approximate generalization to damped oscillations provides a compromise between fully anharmonic dynamics which have no closed form, and harmonics dynamics using Taylor-expanded potential energies, which have a closed form but a limited range of accurate validity: As shown in Fig. S1, the PES computed in Fig. 1 and fourth-order polynomial fit of the PES proposed by Ref. [37] result in accurate frequency shifts as a function of amplitude for large amplitudes (see SM Sec. III). In contrast, aOLAF deviates from the exact solution by only 0.02 THz at a 10 pm amplitude yet by ~0.15 THz at a 20 pm amplitude. In general, the parametrization of the aOLAF protocol through the half periods of the oscillations will be efficient as long as there are no more than one zero-derivative point in the PES crossed over the course of the trajectory, i.e., as long as the energy of the oscillator is smaller than the energy barrier.

III. CONCLUSION

In conclusion, we have quantified the role of anharmonic effects in the lattice response of bismuth and antimony, and proposed a protocol for controlling them. We developed a DFT-informed model of the light-induced lattice dynamics, using an interpolated potential energy surface along the three optical phonon modes. With this model, we investigated the low- and high-amplitude frequencies of light-induced phonons in these materials using a field-dependent, Born-Oppenheimer description of the potential energy surface. We introduced a framework that accurately captures the amplitude-dependent frequency and accumulated phase of the coherent phonon via linearization of the amplitude-dependent frequency of the coherent phonon. The formalism and results presented provide a way to accelerate the calibration of two-pulse experiments and improve the description of protocols for nonlinear phononics.

[1] A. de la Torre, D. M. Kennes, M. Claassen, S. Gerber, J. W. McIver, and M. A. Sentef, *Colloquium:* Nonthermal pathways to ultrafast control in quantum materials, Rev. Mod. Phys. **93**, 041002 (2021).

[2] T. K. Cheng, L. H. Acioli, J. Vidal, H. J. Zeiger, G. Dresselhaus, M. S. Dresselhaus, and E. P. Ippen, Modulation of a semicondutor-to-semimetal transition at 7 THz via coherent lattice vibrations, Appl. Phys. Lett. **62**, 1901 (1993).

[3] A. Anikin, R. D. Schaller, G. P. Wiederrecht, E. R. Margine, I. I. Mazin, and G. Karapetrov, Ultrafast dynamics in the high-symmetry and in the charge density wave phase of $2H$-NbSe$_2$, Phys. Rev. B **102**, 205139 (2020).

[4] R. I. Sharp and E. Warming, The lattice dynamics of antimony, J. Phys. F: Met. Phys. **1**, 570 (1971).

[5] T. K. Cheng, S. D. Brorson, A. S. Kazeroonian, J. S. Moodera, G. Dresselhaus, M. S. Dresselhaus, and E. P. Ippen, Impulsive excitation of coherent phonons observed in reflection in bismuth and antimony, Appl. Phys. Lett. **57**, 1004 (1990).

[6] T. K. Cheng, J. Vidal, H. J. Zeiger, G. Dresselhaus, M. S. Dresselhaus, and E. P. Ippen, Mechanism for displacive excitation of coherent phonons in Sb, Bi, Te, and Ti$_2$O$_3$, Appl. Phys. Lett. **59**, 1923 (1991).

[7] M. Hase, K. Mizoguchi, H. Harima, S. Nakashima, M. Tani, K. Sakai, and M. Hangyo, Optical control of coherent optical phonons in bismuth films, Appl. Phys. Lett. **69**, 2474 (1996).

[8] G. A. Garrett, T. F. Albrecht, J. F. Whitaker, and R. Merlin, Coherent THz phonons driven by light pulses and the Sb problem: What is the mechanism? Phys. Rev. Lett. **77**, 3661 (1996).

[9] M. Hase, K. Mizoguchi, H. Harima, S. I. Nakashima, and K. Sakai, Dynamics of coherent phonons in bismuth generated by ultrashort laser pulses, Phys. Rev. B **58**, 5448 (1998).

[10] M. F. DeCamp, D. A. Reis, P. H. Bucksbaum, and R. Merlin, Dynamics and coherent control of high-amplitude optical phonons in bismuth, Phys. Rev. B **64**, 092301 (2001).

[11] M. Hase, M. Kitajima, S. I. Nakashima, and K. Mizoguchi, Dynamics of coherent anharmonic phonons in bismuth using high density photoexcitation, Phys. Rev. Lett. **88**, 067401 (2002).

[12] T. Dekorsky, W. Kütt, T. Pfeifer, and H. Kurz, Coherent control of LO-phonon dynamics in opaque semiconductors by femtosecond laser pulses, Europhys. Lett. **23**, 223 (1993).

[13] M. Taghinejad, Z. Xu, K.-T. Lee, T. Lian, and W. Cai, Transient second-order nonlinear media: Breaking the spatial symmetry in the time domain via hot-electron transfer, Phys. Rev. Lett. **124**, 013901 (2020).

[14] A. Haldar, C. L. Cortes, S. K. Gray, S. Sharifzadeh, and P. Darancet, Giant optomechanical coupling in the charge density wave state of tantalum disulfide, arXiv:2105.08874.

[15] G. Khalsa, N. A. Benedek, and J. Moses, Ultrafast control of material optical properties via the infrared resonant Raman effect, Phys. Rev. X **11**, 021067 (2021).

[16] R. Merlin, Generating coherent THz phonons with light pulses, Solid State Commun. **102**, 207 (1997).

[17] *Raman Scattering in Materials Science*, edited by W. H. Weber, R. Merlin, A. Zunger, R. M. Osgood, R. Hull, and H. Sakaki, Springer Series in Materials Science Vol. 42 (Springer, Berlin, 2000).

[18] T. Dekorsy, H. Auer, C. Waschke, H. J. Bakker, H. G. Roskos, H. Kurz, V. Wagner, and P. Grosse, Emission of submillimeter electromagnetic waves by coherent phonons, Phys. Rev. Lett. **74**, 738 (1995).

[19] A. Subedi, A. Cavalleri, and A. Georges, Theory of nonlinear phononics for coherent light control of solids, Phys. Rev. B **89**, 220301(R) (2014).

[20] H. J. Zeiger, J. Vidal, T. K. Cheng, E. P. Ippen, G. Dresselhaus, and M. S. Dresselhaus, Theory for displacive excitation of coherent phonons, Phys. Rev. B **45**, 768 (1992).

[21] T. E. Stevens, J. Kuhl, and R. Merlin, Coherent phonon generation and the two stimulated Raman tensors, Phys. Rev. B **65**, 144304 (2002).

[22] J. Lloyd-Hughes, P. M. Oppeneer, T. Pereira Dos Santos, A. Schleife, S. Meng, M. A. Sentef, M. Ruggenthaler, A. Rubio, I. Radu, M. Murnane, X. Shi, H. Kapteyn, B. Stadtmüller, K. M. Dani, F. H. Da Jornada, E. Prinz, M. Aeschlimann, R. L. Milot, M. Burdanova, J. Boland *et al.*, The 2021 ultrafast spectroscopic probes of condensed matter roadmap, J. Phys.: Condens. Matter **33**, 353001 (2021).

[23] J. Xu, D. Chen, and S. Meng, Decoupled ultrafast electronic and structural phase transitions in photoexcited monoclinic VO$_2$, Sci. Adv. **8**, eadd2392 (2022).

[24] É. D. Murray, D. M. Fritz, J. K. Wahlstrand, S. Fahy, and D. A. Reis, Effect of lattice anharmonicity on high-amplitude phonon dynamics in photoexcited bismuth, Phys. Rev. B **72**, 060301(R) (2005).

[25] É. D. Murray, S. Fahy, D. Prendergast, T. Ogitsu, D. M. Fritz, and D. A. Reis, Phonon dispersion relations and softening in photoexcited bismuth from first principles, Phys. Rev. B **75**, 184301 (2007).

[26] E. Papalazarou, J. Faure, J. Mauchain, M. Marsi, A. Taleb-Ibrahimi, I. Reshetnyak, A. van Roekeghem, I. Timrov, N. Vast, B. Arnaud, and L. Perfetti, Coherent phonon coupling to individual Bloch states in photoexcited bismuth, Phys. Rev. Lett. **108**, 256808 (2012).

[27] O. V. Misochko, Experimental evidence of the existence of a nonstationary coherent crystal state in bismuth, J. Exp. Theor. Phys. **118**, 227 (2014).

[28] J. P. Perdew, M. Ernzerhof, and K. Burke, Rationale for mixing exact exchange with density functional approximations, J. Chem. Phys. **105**, 9982 (1996).

[29] J. Enkovaara, C. Rostgaard, J. J. Mortensen, J. Chen, M. Dułak, L. Ferrighi, J. Gavnholt, C. Glinsvad, V. Haikola, H. A. Hansen, H. H. Kristoffersen, M. Kuisma, A. H. Larsen, L. Lehtovaara, M. Ljungberg, O. Lopez-Acevedo, P. G. Moses, J. Ojanen, T. Olsen, V. Petzold *et al.*, Electronic structure calculations with GPAW: A real-space implementation of the projector

augmented-wave method, J. Phys.: Condens. Matter **22**, 253202 (2010).

[30] A. Hjorth Larsen, J. Jørgen Mortensen, J. Blomqvist, I. E. Castelli, R. Christensen, M. Dułak, J. Friis, M. N. Groves, B. Hammer, C. Hargus, E. D. Hermes, P. C. Jennings, P. Bjerre Jensen, J. Kermode, J. R. Kitchin, E. Leonhard Kolsbjerg, J. Kubal, K. Kaasbjerg, S. Lysgaard, J. Bergmann Maronsson *et al.*, The atomic simulation environment—a Python library for working with atoms, J. Phys.: Condens. Matter **29**, 273002 (2017).

[31] N. Marzari, D. Vanderbilt, A. De Vita, and M. C. Payne, Thermal contraction and disordering of the Al(110) surface, Phys. Rev. Lett. **82**, 3296 (1999).

[32] See Supplemental Material at http://link.aps.org/supplemental/10.1103/PhysRevMaterials.8.015202 for computational details, implementation of the propagator, comparison of amplitude-dependent for OLAF and other methods, details of the linearization protocol, choice of units used in the scripts, details of the Raman measurements, and the momentum- and frequency-resolved dielectric response of Bi and Sb.

[33] P. Virtanen, R. Gommers, T. E. Oliphant, M. Haberland, T. Reddy, D. Cournapeau, E. Burovski, P. Peterson, W. Weckesser, J. Bright, S. J. Van Der Walt, M. Brett, J. Wilson, K. J. Millman, N. Mayorov, A. R. J. Nelson, E. Jones, R. Kern, E. Larson, C. J. Carey *et al.*, SciPy 1.0: Fundamental algorithms for scientific computing in Python, Nat. Methods **17**, 261 (2020).

[34] J. S. Lannin, J. M. Calleja, and M. Cardona, Second-order Raman scattering in the group- V_b semimetals: Bi, Sb, and As, Phys. Rev. B **12**, 585 (1975).

[35] F. Sun, Q. Wu, Y. L. Wu, H. Zhao, C. J. Yi, Y. C. Tian, H. W. Liu, Y. G. Shi, H. Ding, X. Dai, P. Richard, and J. Zhao, Coherent helix vacancy phonon and its ultrafast dynamics waning in topological Dirac semimetal Cd_3As_2, Phys. Rev. B **95**, 235108 (2017).

[36] T. Dekorsy, G. C. Cho, and H. Kurz, Coherent phonons in condensed media, in *Light Scattering in Solids VIII*, edited by M. Cardona and G. Güntherodt, Topics in Applied Physics Vol. 76 (Springer, Berlin, 2000), pp. 169–209.

[37] F. Iyikanat, A. Konečná, and F. J. García De Abajo, Nonlinear tunable vibrational response in hexagonal boron nitride, ACS Nano **15**, 13415 (2021).

[38] H. H. Denman, Amplitude-dependence of frequency in a linear approximation to the simple pendulum equation, Am. J. Phys. **27**, 524 (1959).